CR 137912

THE UNIVERSITY OF NEW MEXICO
COLLEGE OF ENGINEERING
BUREAU OF ENGINEERING RESEARCH
ALBUQUERQUE, NEW MEXICO

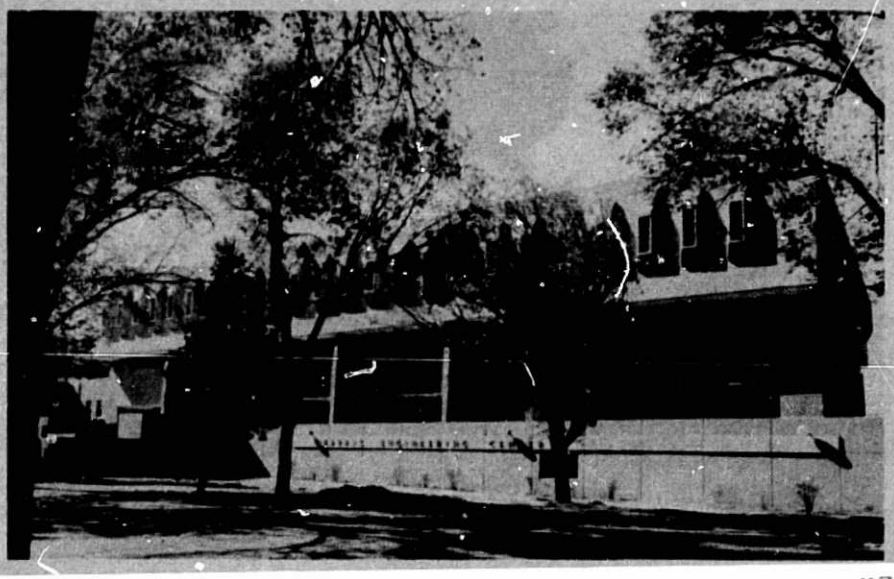

INVESTIGATION OF PERFORMANCE LIMITS IN AXIAL GROOVE HEAT PIPES

by

K. Thomas Feldman

Final Report

UNM Technical Report ME-79(76)NASA-365-1
NASA CR 137,912

July 1976

This work was supported by NASA Grant NSG-2064

NASA CR 137,912

Final Report

on

"INVESTIGATION OF PERFORMANCE LIMITS IN AXIAL GROOVE HEAT PIPES"

NASA Grant No. NSG-2064

to

NASA Ames Research Center
Moffett Field, California 94035

by

K. Thomas Feldman
Professor

The University of New Mexico
The Bureau of Engineering Research
and
The Department of Mechanical Engineering
Albuquerque, New Mexico 87131

UNM Technical Report ME-70(76)NASA-365-1

July 1976

ABSTRACT

In this study the entrainment-shear performance limit which occurs in axial groove heat pipes was investigated and explained. In the existing heat pipe literature the entrainment heat flux limit is defined as the condition where the Weber number is greater than or equal to one. In this analysis, the critical value for the entrainment Weber number is found to be $2\pi \leq We \leq 3\pi$. Perhaps more important to the heat pipe designer than the entrainment performance limit is the prediction of the performance degradation due to vapor-liquid shearing stress which is also described. Preliminary qualitative experiments were conducted to observe the shear stress wave formation phenomena. Further more elaborate experiments would provide valuable verification of the shear stress wave phenomena and of associated performance degradation and limits. The equations presented in this analysis may be used to predict and minimize the vapor-liquid shear stress performance effects that occur in axial groove and puddle flow artery heat pipes.

ACKNOWLEDGEMENTS

The work described in this report was performed under NASA Grant NSG-2064. Dr. Craig R. McCreight of NASA Ames Research Center served as the grant technical monitor. The author would like to express appreciation for a substantial amount of help from Dr. Chowna Thupvongsa, Research Assistant, and from Mrs. Jennie Scales, Mrs. Janet Smith and Mrs. Joyce Meyer of the Bureau of Engineering Research who helped reproduce this report.

TABLE OF CONTENTS

NOMENCLATURE

A_v	Vapor flow area, m^2
A_ℓ	Liquid flow area, m^2
$\bar{A}_\ell$	Averaged liquid flow area, m^2
C	Wave velocity, m/s
C_o	Wave velocity in absence of current, m/s
D_h	Hydraulic diameter, 4A/P
D_v	Internal pipe flow diameter, m
d	Characteristic dimension, m
f	Frequency, cycle/s
f_L	Friction factor for liquid flow in groove
f_{LP}	Friction factor for liquid flow in circular tube
f_v	Friction factor for vapor flow
G_v	Total vapor flow rate per pipe flow area, kg/m^2s
h_{fg}	Specific latent heat enthalpy, J/kg
K	Wick permeability, m^2
L_{eff}	Heat pipe effective length, m
ℓ_m	Characteristic mixing length, m
ℓ''	Half-width of zone of influence at interface, m
m	Wave number, $2\pi/\lambda$
N	Number of pipe grooves
N_ℓ	Liquid transport factor
Δp_s	Capillary pumping pressure rise, N/m^2
Δp_ℓ	Pressure drop in the liquid, N/m^2
$\Delta p_{\ell,o}$	Pressure drop in the liquid due to viscosity, N/m^2
$\Delta p_{\ell,v}$	Pressure drop in the liquid induced by counterflow, N/m^2
Δp_v	Pressure drop in the vapor, N/m^2
p_v	Vapor pressure, N/m^2
p_ℓ	Liquid pressure, N/m^2
P	Wetted perimeter of the fluid flow passage, m

$\dot{Q}$	Heat transfer rate, watts
r_p	Effective pumping radius, m
Re	Reynolds number
S	Dimensionless shear stress at vapor liquid interface, $(\delta\tau_w)/(\mu_\ell U_\ell)$
s	Width of land between grooves, m
$U_{v\ell}$	Relative vapor-liquid velocity, m/s
U_v	Axial vapor velocity, m/s
U_ℓ	Liquid velocity, m/s
w	Groove width, m
We	Weber number, dimensionless
x	Coordinate parallel to mean flow, m
y	Coordinate perpendicular to mean flow, m

Greek letter nomenclature

β	Disturbance growth factor, s^{-1}
δ	Film thickness or groove depth, m
η_o	Amplitude of the surface wave, m
ϕ	Aspect ratio of capillary grooves, $w/2\delta$
λ	Wavelength, m
μ_ℓ	Liquid dynamic viscosity, Ns/m^2
μ_v	Vapor dynamic viscosity, Ns/m^2
ν_ℓ	Liquid kinematic viscosity, m^2/s
ν_v	Vapor kinematic viscosity, m^2/s
ρ_ℓ	Liquid density Kg/m^3
ρ_v	Vapor density, Kg/m^3
σ	Surface tension, N/m
τ_w	Shear stress created by the vapor on the liquid at its free surface, N/m^2
ω	Radian frequency of interfacial waves, sec^{-1}

INVESTIGATION OF PERFORMANCE LIMITS IN AXIAL GROOVE HEAT PIPES

1.0 Introduction

A survey of the various types of heat pipes used by NASA, ERDA, and industrial companies indicates a recent preference for configurations of axial and circumferential groove wick designs.[1] Such groove wick heat pipes, have the advantages of high evaporation and condensation film coefficients, reliable operation, ease of manufacturing, and potentially low cost.

However, in operating the groove wick heat pipe, a number of performance limits are encountered. Since the groove wick heat pipe is normally not used with additional screen wick, there is a significant counterflow shear interaction between the vapor and liquid. The resulting pressure drop associated with this counterflow vapor-liquid shear results in lower than maximum heat transfer rates and in some cases unstable operation due to slugging or other entrainment-shear phenomena of the liquid. When operated in a gravity environment, the axial groove heat pipe may have a puddle of excess liquid accumulate along the lower side of the pipe. Counterflow shear and entrainment of liquid from the unshielded surface of the puddle can occur at relatively modest heat transfer rates.

Also, while operating in a 1-g environment, the axial groove heat pipe can experience desaturation of the upper grooves along the top of the pipe. Depending on the construction of the grooves, these upper grooves may experience an additional hydrodynamic stress, which will cause them to first dry out the upper side of the evaporator. Heat pipe performance is thereby restricted by this capillary limit in the grooves. Since these limits are not fully understood for axial groove or circumferential groove heat pipes, the expected heat flux limits and evaporation and condensation film coefficients needed for design of various groove geometries are not well known at this time.

Because of these factors, a research project was initiated at The University of New Mexico to investigate the vapor-liquid shear and entrainment performance limits of the axial groove heat pipe. This project was supported by the NASA Ames Research Center on Contract No. NSG-2064 over the period from January 20, 1975 through January 19, 1976.

2.0 Previous Research

A modest amount of previous research has been done on the problem of counterflow vapor-liquid entrainment-shear limits. A theoretical study was reported in 1968 by Bähr, Burck, and Hufschmidt[2] to predict friction factors and pressure drops associated with counter flow vapor-liquid shear. Also in this paper, they described experimental work with water-air interactions which had been initiated. A companion paper published in 1969 by Hufschmidt, Burck, DiCola, and Hoffman[3] gives a detailed summary of the theoretical analysis results, and a comparison with the experimental data.

The theory was originally developed by DiCola[4] assuming laminar flow of liquid in a rectangular open top channel with a counterflow vapor shear at the surface. The friction factor increase due to the vapor shear over that for Poiseuille of liquid in a tube was given by the ratio

$$\frac{f_L}{f_{LP}} = \left(\frac{f_L}{f_{LP}}\right)_o \left(1 + \frac{\phi^2 S}{3}\right), \qquad \phi < 0.5 \tag{2.1}$$

where S is the nondimensional stress, defined as $\frac{\delta\, \tau_w}{\mu_\ell\, U_\ell}$, and

$$\left(\frac{f_L}{f_{LP}}\right)_o = \frac{3}{2(1+\phi)^2(1-0.627\,\phi)} \tag{2.2}$$

is the friction factor ratio for S = 0, zero vapor shear, ($\tau_w = 0$).

For a heat pipe with N rectangular grooves of cross-section δw and $A_\ell = \delta w N$ the interface shear stress was given by

$$S = \frac{2\, N \delta^2 w}{D_h^2 P} \frac{\nu_v}{\nu_\ell} \left(f_v Re_v\right) \tag{2.3}$$

where the symbols are defined in the nomenclature list.

Florschuetz[5] has taken these results and applied them to the performance of a sodium heat pipe and a water heat pipe both having open axial grooves. For both heat pipes the effect of vapor shear was found to reduce the heat transfer rate significantly at low vapor pressures.

A related paper by Zimmermann[6] also deals with the counterflow shear friction factor and pressure drop in heat pipes.

Another paper dealing with the counterflow shearing limit in the 0 - g environment is by Schlitt, et al.[7] The maximum heat transport is determined from the relationship

$$\Delta p_s = \Delta p_\ell + \Delta p_v \ . \tag{2.4}$$

The liquid pressure drop consists of two terms,

$$\Delta p_\ell = \Delta p_{\ell,c} + \Delta p_{\ell,v} \tag{2.5}$$

where $\Delta p_{\ell,c}$ is the viscous loss associated with the flowing liquid and applies to all capillary channels. The second term, $\Delta p_{\ell,v}$, is the pressure drop in the liquid that is induced by the shearing action of the vapor counterflow and applies to open channels.

The individual pressure drop ratios were given as

$$\frac{\Delta p_{\ell,c}}{\Delta p_s} = \frac{\dot{Q} L_{eff}}{N_\ell} \frac{r_p}{KA_\ell} \tag{2.6}$$

$$\frac{\Delta p_{\ell,v}}{\Delta p_s} = \frac{\dot{Q} L_{eff}}{N_\ell} \frac{r_p}{KA_\ell} \left[\frac{1}{24} \frac{\nu_v}{\nu_\ell} \frac{(w/D_v)^2}{(1+s/w)} f_v \, Re_v \right] \tag{2.7}$$

$$\frac{\Delta p_v}{\Delta p_s} = \frac{\dot{Q} L_{eff}}{N_\ell} \frac{r_p}{KA_\ell} \left[\frac{1}{24} \frac{\nu_v}{\nu_\ell} \frac{KA_\ell}{D_v^2 A_v} f_v \, Re_v \right] \tag{2.8}$$

where

$$f_v = \begin{cases} 64/Re_v & \text{laminar vapor flow} \\ 0.316/Re_v^{1/4} & \text{turbulent vapor flow} \end{cases} \tag{2.9}$$

and $$K = \frac{D_{h,\ell}^2}{(2 f_\ell \, Re_\ell)} \tag{2.10}$$

For the groove geometry given in Figure 1,

$$D_{h,\ell} = \frac{4A}{2\delta + w} \tag{2.11}$$

and

$$f_\ell \, Re_\ell = f(w/\delta) = 15 \tag{2.12}$$

The Equations 2.4, 2.5, 2.6 2.7, 2.8, and 2.9 can be combined to solve for the 0-g transport capability. The averaged liquid groove area was used which accounts for an average liquid meniscus recession.

$$\bar{A}_\ell = A_\ell - N\left(\frac{1}{4}\frac{\pi w^2}{4}\right) \tag{2.13}$$

The presence of the $f_v Re_v$ terms in Equations 2.7 and 2.8 makes it difficult to solve for the heat transport rate explicitly, particularly for turbulent flow where the Reynolds number has an exponent as given in Equation 2.9. A simpler formulation for predicting the shearing heat flux limit is needed for an explicit solution.

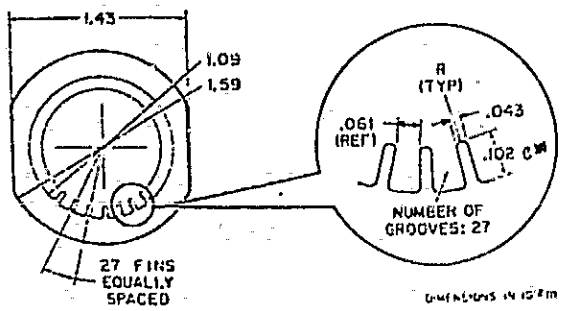

Fig. 1. Cross section of axial grooved aluminum extrusion.

Also, a brief theoretical analysis of two-phase flow interactions is given in the book by G. B. Wallis.[8] However, none of these studies includes a thorough investigation of the entrainment interaction where waves and liquid droplets are formed.

At the present time, in heat pipe design it is common to treat prediction of the entrainment based on prior knowledge of a "characteristic dimension" in the heat pipe.[9,10] Entrainment is presumed to occur when the inertial vapor forces exceeded the liquid surface tension forces at the vapor-liquid interface. The ratio of these forces is expressed by the Weber number

$$We = \frac{\rho_v U_v^2 d}{\sigma} \tag{2.14}$$

where d = characteristic dimension such as the space between wires in a screen wick heat pipe.

Cotter[9] stated this in a slightly different way. He stated that the wavelength λ of a small disturbance on the liquid surface will grow in amplitude exponentially with time if,

$$We = \frac{\rho_v U_v^2 \lambda}{2\pi} > 1. \tag{2.15}$$

> "The process continues until the amplitude transcends the validity of the linear theory, and presumably ends in stripping of liquid droplets from the crests of the undulations. The quantity on the left is the Weber number with characteristic dimension $\lambda/2\pi$, which is a geometric property of the capillary structure in the interface region." (Ref. 9, p. 347)

Note here that Cotter's Weber number may be rearranged,

$$We = \frac{\rho_v U_v^2 \lambda}{\sigma} > 2\pi \tag{2.16}$$

Later Kemme[10] pointed out that the "entrainment heat flux limit," $\dot{Q}_{ent}/A_v$, is obtained by setting the Weber number equal to one, and combining it with

$$\dot{m} = \rho_v U_v A_v \text{ and } \dot{Q} = \dot{m}\, h_{fg},$$

$$\frac{\dot{Q}_{ent}}{A_v} = \sqrt{\frac{\bar{\rho}_{ev}\, \sigma h_{fg}^2}{d}} \tag{2.17}$$

where

$\bar{\rho}_{ev}$ = mean vapor density at the evaporator exit.

Equation 2.17 has been used to predict entrainment limit heat fluxes, by assuming a value for the characteristic dimension d. However, some investigators have correlated this entrainment limit with d equal to the space between wires while others use the wire diameter. Obviously, there is a need for better understanding the entrainment phenomenon and to clarify the use of the characteristic dimension d.

3.0 WAVE FORMATION AND ENTRAINMENT

Since the previous research just described has defined the friction factors suitable for use in predicting increased pressure drop in axial groove heat pipes but has not considered the unstable effects of waves, ripples, or entrainment droplet formation, the work presented in this report is focused primarily on the latter phenomena. Also, a discussion is presented to help clarify the use of the wave length, λ, the characteristic dimension, d, the Weber number, and the entrainment-shear heat transfer rate limit.

Hanratty, et al.[11,12] have conducted both theoretical and experimental studies on the initiation of waves due to the flow of gas or vapor over liquid. Parts of the results of these studies have been incorporated in the following discussion. Suppose a liquid is flowing in one direction in a gently downward sloping open channel and its vapor is flowing over it in the opposite direction, as shown in Figure 2. At zero or very low vapor velocity, the flowing liquid will be undisturbed, however, with increasing relative velocity, a destabilizing effect is noted. The first waves to appear are small two-dimensional ripples which extend over the width of the channel and travel in the direction of the vapor flow. At even higher vapor velocity the amplitude and the wave velocity increases and a three-dimensional cross-hatched wave pattern appears. This latter case is similar to the waves which are obtained on a body of water during a light squall.

At a vapor velocity which is about double that necessary to produce the cross-hatched waves, the first roll waves appear. The roll waves occur when the crests of the waves are moving faster than the troughs. This causes the downstream end of a wave to steepen and to roll over upon itself. Thus, liquid in the wave is moving in a circular path. Such waves are called roll waves. They were first described by Cornish[13] who observed them in mountain streams. A good review of the literature on this topic is given by Hanratty.[12] The first theoretical prediction for the conditions causing roll waves was made by Jeffreys[14] who considered the case of turbulent flow in an open inclined channel.

At higher vapor velocity the shear forces on the tops of the roll waves and the natural rolling action of the waves are adequate to overcome the surface tension forces of the liquid so droplets of liquid are

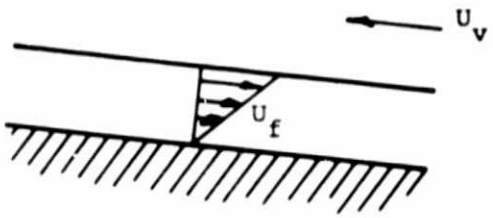

a) Undisturbed liquid

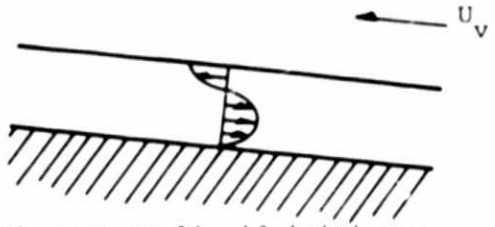

b) Drag on liquid initiates flow reversal at surface, and ripple waves are formed.

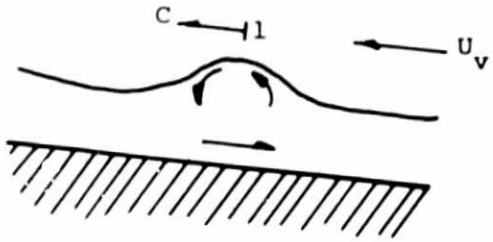

c) Initiation of roll waves

c) Roll waves, fully developed.

e) Initiation of droplet entrainment and "white water."

Fig. 2. Subsequent wave phenomena

separated from the surface and entrained into the vapor stream. The onset of droplet entrainment is usually preceded by a noticeable roughening of the tops of the roll waves which resembles patches of "white water." Further increases of vapor flow velocity increase the entrainment.

The sequence of events in the entrainment process is shown in Figure 2. The corresponding regions of wave activity are shown in Figure 3 for an experiment conducted by Wallis, et al. in which air flowed over water in a horizontal duct 30 cm (12 inches) wide and 12.7 cm (5 inches) deep.[15]

In a heat pipe the onset of entrainment may be encouraged by nucleate boiling in the evaporator which can occur at sufficiently high heat fluxes. The bursting of bubbles at the liquid surface, as shown in Figure 4, has long been known as a source of droplet entrainment.[16]

In order to help elucidate the phenomena of wave formation and entrainment, the following definitions of terms are given:

1. Ripple Waves: Two-dimensional waves formed by gentle undulations of low amplitude (less than 0.1 mm, 0.005 inches) on the liquid surface which travel at about 22-30 cm/sec (0.75 to 1.00 feet/sec) in an air-water system, and are not initiated by turbulence in the vapor flow.

2. Cross-hatched Waves: As the vapor velocity is increased slightly these three-dimensional waves appear as a criss-cross ripple or as a pebbled pattern. For an air-water system the wave lengths are of the order of 0.5-1 cm (0.25-0.5 inches) and the waves travel at only slightly greater velocity than the ripple waves.

3. Roll Waves: As the vapor velocity is increased the cross-hatched waves become stable and persist up to a vapor velocity about double that necessary to produce the cross-hatched waves. At this point, roll waves appear and travel at about 60 cm/sec (2 ft/sec) down the channel. The roll waves may take a finite distance along the channel to form and normally they appear first where the film depth is a maximum.

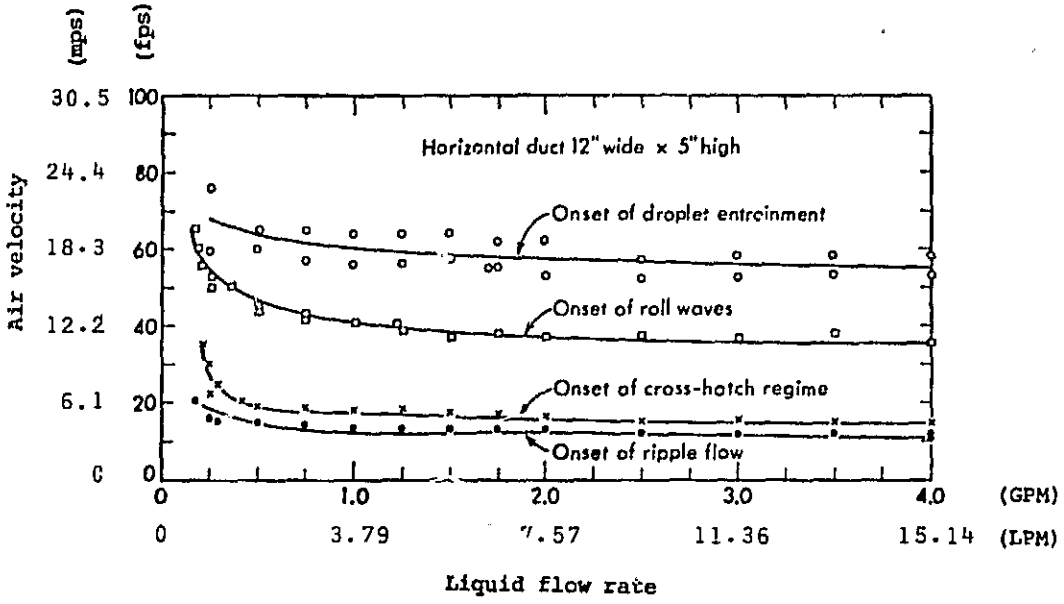

Fig. 3. Regions of wave activity in stratified air-water flow[15]

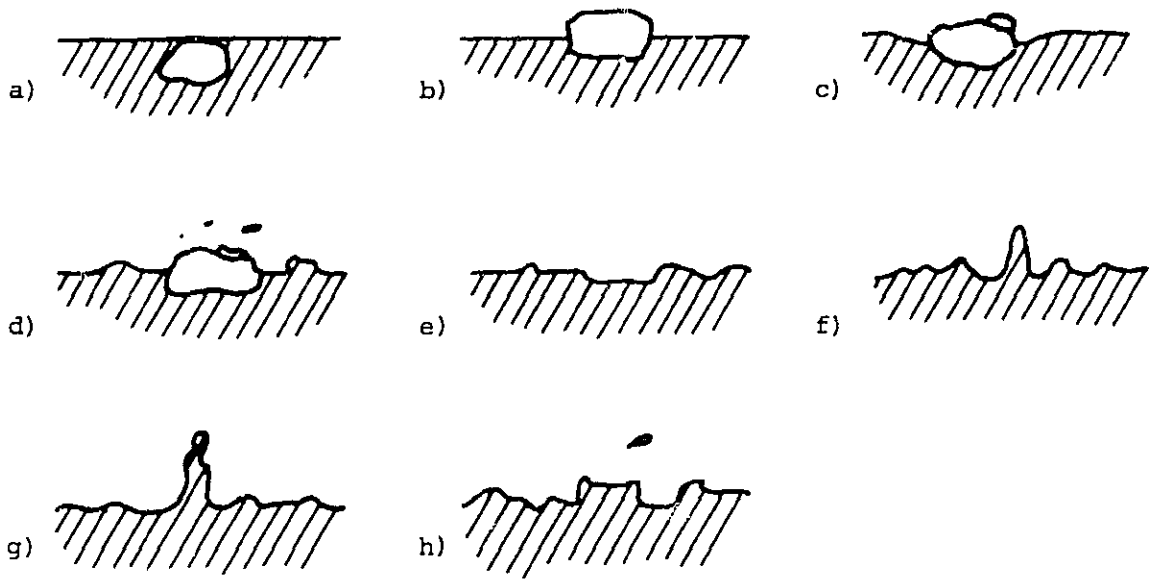

Fig. 4. Mechanism of droplet entrainment resulting from the emission of a bubble from a liquid surface[16]

4. Droplet Entrainment: Further increases of vapor velocity, up to about 50 percent more than that needed to produce roll waves, will cause droplets to be torn from the liquid surface and entrained into the vapor flow.

4.0 EXPERIMENTAL OBSERVATIONS

In order to observe the entrainment-shear interactions, three different experimental heat pipes were built and preliminary qualitative observation tests were conducted. A schematic drawing of the final apparatus is shown in Figure 5 and a photo is shown in Figure 6. The apparatus is composed of an axial grooved copper tube with a 91.4 cm (3 foot) evaporator and condenser section, and a 15.24 cm (6 inch) glass tube adiabatic transport section. Each end of the tube has glass observation windows for viewing phenomena along the axis.

In the experimental tests Freon-12 was used as the working fluid since it has a low latent heat of vaporization which will give large mass flow rates at modest heat transfer rates. With the heat pipe in a horizontal orientation, the evaporator would experience nucleate boiling and dryout before any wave phenomena were observed in the adiabatic transport section. By raising the condenser end 1.27 cm (1/2 inch), and by adding cooling water over the condenser to lower the pipe temperature to 27°C (80°F), waves were observed in the adiabatic transport section, as shown in Figure 7. The average wavelength of the waves observed was approximately 0.4 cm (0.157 inches). Also, in Figure 8, a sketch of the observed wave phenomena is shown. The waves gradually increase in amplitude down the tube from the boiling wave source in the evaporator and become fully developed in the adiabatic transport section and gradually die down as they enter the condenser section. Further increasing of the condenser elevation, evaporator heat input rate, and a slight reduction of the condenser temperature showed a slight increase in wave speed but no entrainment was observed. Insufficient time and equipment prevented further qualitative experiments. A chilled liquid cooling unit was ordered, but was not received in time to conduct tests at lower temperatures. One would expect that some entrainment could be observed at lower temperatures where the vapor pressures and densities are lower and the entrainment limit is lower.

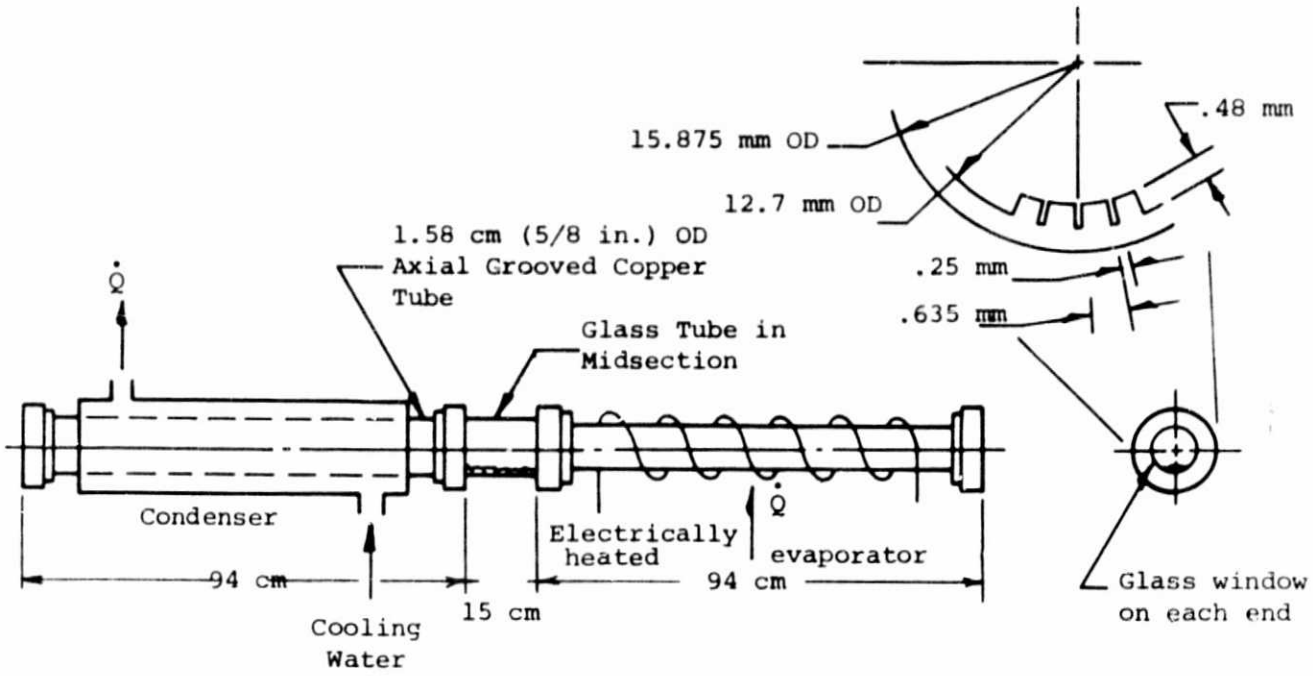

Fig. 5. Sketch of experimental apparatus

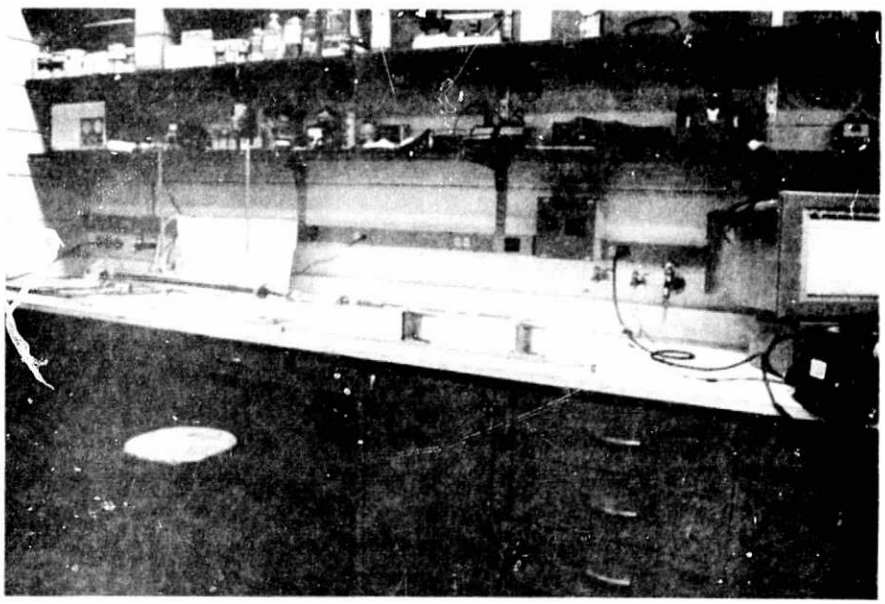

Fig. 6. Photograph of experimental apparatus

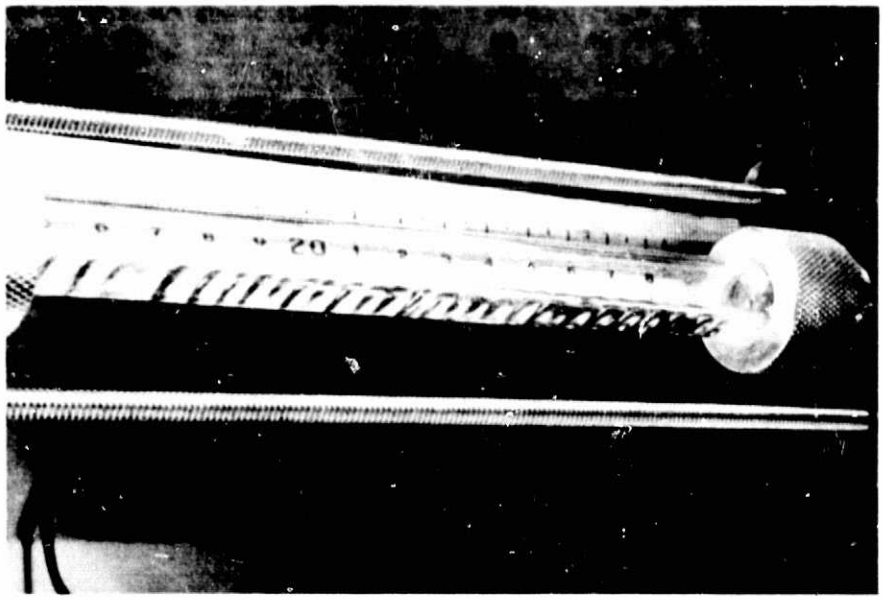

Fig. 7. Photograph of waves observed in the adiabatic transport section. (The evaporator is at the right hand side of the photo.)

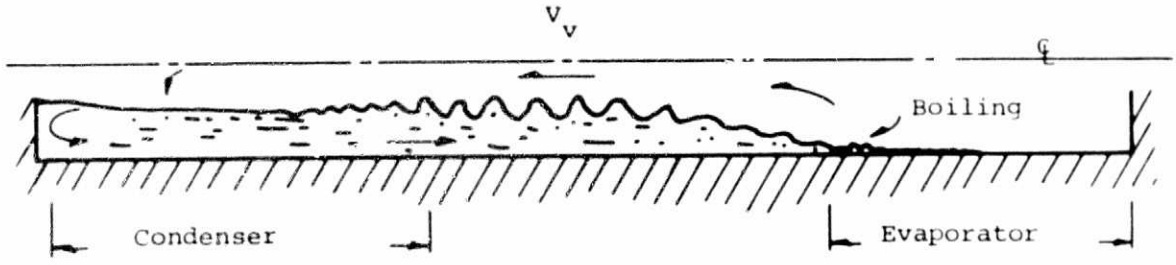

Fig. 8. Sketch of wave phenomena observed

5.0 HYDRODYNAMIC WAVE INSTABILITY

The hydrodynamic instability of waves formed on a liquid surface by gas or vapor flow over it may be explained physically as follows. As the surface film is disturbed from its equilibrium position, normal and tangential stresses are produced and waves will form. The normal stress component is in phase with the wave displacement, and it attempts to deform the liquid surface by exerting an upward force on the crests and a downward force on the troughs of small periodic waves. Also, the tangential stress component is in phase with the wave slope, and it has the effect of accelerating the liquid on the windward slope while retarding that on the leeward slope. The latter mechanism tends to displace fluid towards the crests and away from the troughs of the waves, thereby increasing their amplitude.

The crests of the long wavelength disturbances on a flowing liquid move faster than their troughs and this causes the downstream part of the wave to steepen and roll over upon itself. The thinner the liquid film, the more effective this mechanism is, for in very thin films, the perturbation velocity in the horizontal direction is much greater than in the vertical, so the influence of the tangential and vertical stresses extends throughout the whole film. The development of waves is governed by continuity conditions. The wave growth rate is proportional to the rate of accumulation of liquid near the crests, and this, in turn, is inversely proportional to the liquid viscosity.

Wave instabilities grow when the disturbing vapor stress is sufficient to overcome the restoring forces of gravity and surface tension. With a given vapor flow rate, instabilities can always be induced in an initially stable film by decreasing its thickness. Also, increasing the liquid flow velocity simply increases the roll wave frequency.

5.1 Analysis of the Wave Instability

As is shown in Figure 9, the wave flow along the surface of a liquid film caused by a vapor flow may be considered to be a sinusoidal wave moving at speed C. Analysis of the problem is simplified by using a coordinate system moving at the speed U_ℓ, so that the liquid flow velocity, U_ℓ, is zero and the relative vapor velocity is $U_{v\ell} = U_{v\ell} + U_\ell$.

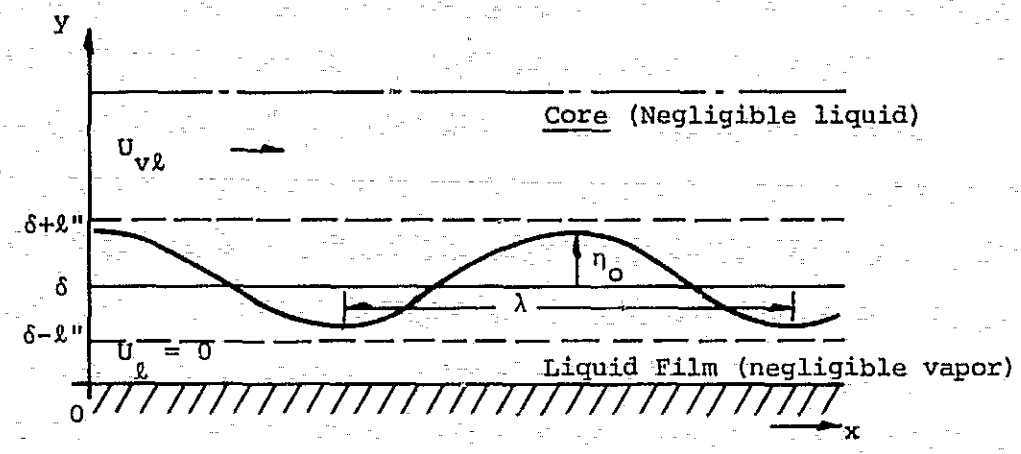

Fig. 9. System for film stability analysis.

The dynamic equation for the surface wave given by Tippets[17] is

$$\ddot{\eta}_o - \beta^2 \eta_o = 0 \tag{5.1}$$

where η_o is the amplitude of the surface wave as shown in Figure 9 and β is a disturbance growth parameter given by

$$\beta = \frac{(\omega - mU_{v\ell})^2 \tanh(m\ell'') + \frac{\rho_\ell}{\rho_v}\omega^2 \coth(m\delta) - \sigma m^3/\rho_v}{\frac{\rho_\ell}{\rho_v}\coth(m\delta) + \tanh(m\ell'')} \tag{5.2}$$

and the radian frequency of the interfacial waves is

$$\omega = \frac{mU_{r\ell}}{1 + \frac{\rho_\ell}{\rho_v}\frac{\coth(m\delta)}{\tanh(m\ell'')}} \tag{5.3}$$

The vapor-liquid interface will grow indefinitely with time if $\beta^2 > 0$. The critical wavelength, for $\beta = 0$, is given by

$$\lambda_c = \frac{2\pi\sigma}{\rho_v U_{v\ell}^2}\left(1 + \frac{\rho_v}{\rho_\ell}\right). \tag{5.4}$$

The fastest growing disturbances are those having a wavelength λ_m which maximizes the growth factor β, which is given by

$$\lambda_m = \frac{3\pi\sigma}{\rho_v U_{v\ell}^2}\left(1 + \frac{\rho_v}{\rho_\ell}\right) \tag{5.5}$$

In obtaining these results Tippets[17] assumed that the fluid is in potential flow. This idealization approximates the condition of well developed turbulence at the interface. He related the wavelength and film thickness at instability to the common properties of the flow, under the assumption that the interfacial wave motion is dominated by the stream turbulence. He used Prandtl's mixing length theory to relate the turbulent shear stress $\tau = -\overline{\rho U'v'}$ to the local mean flow properties by a characteristic mixing length ℓ_m. This analysis assumes that the surface wavelength, λ, is proportional to ℓ_m, ℓ'', and to the film thickness, δ. He further explained that due to the character of turbulent flow there exists a spectrum of possible disturbance wavelengths extending from near the dimensions of the molecular motion up to within an order of magnitude of the duct dimensions. Disturbances with wavelengths $\lambda < \lambda_c$ can be ignored, since their amplitude will remain small. Disturbances with wavelengths $\lambda > \lambda_m$ can also be ignored, because their growth rates will be no faster than those with wavelengths slightly less than λ_m. Thus, the dominant wavelength λ_o of the characteristic disturbance motion impressed on the interface by the turbulence is bounded according to $\lambda_c < \lambda_o < \lambda_m$. Hence, from Equations 5.4 and 5.5

$$\lambda_o = \frac{K_3\sigma}{\rho_v U_{v\ell}^2}\left(1 + \frac{\rho_v}{\rho_\ell}\right) \qquad 2\pi < K_3 < 3\pi. \tag{5.6}$$

The corresponding film thickness is

$$\delta = (K_3/K_1)\,\frac{\sigma}{\rho_v U_{v\ell}^2}\left(1 + \frac{\rho_v}{\rho_\ell}\right) \tag{5.7}$$

where K_1 is defined by $\lambda_o = K_1\delta$, and $K_1 \approx 1.0$.

The entrainment begins after the initiation of the instability if the disturbance wavelength is within the λ_o range. The occurrance of entrainment reduces the liquid film thickness. When the film thickness is reduced the wave disturbances are reduced, thereby reducing the entrainment. Thus, the wavelength and film thickness will tend to stabilize about the values given by Equations 5.6 and 5.7.

Heat transfer by evaporation from the liquid layer may be included in the above analysis. However, boiling heat transfer cannot be included since the forces on the film associated with boiling bubbles have not been incorporated in the analysis. It would be expected that liquid films on high heat flux surfaces where boiling occurs would tend to be thinner than that predicted by Equation 5.7.

5.1.1 Weber Number Relationship

We can write the Weber number, previously given by Equation 2.14, as

$$We = \frac{\rho_v U_{v\ell}^2 \lambda_o}{\sigma} \tag{5.8}$$

where λ_o is used for the characteristic dimension, in place of d. We now note that if Equation 5.6 is arranged as

$$\frac{\rho_v U_{v\ell}^2 \lambda_o}{\sigma} = K_3(1 + \rho_v/\rho_\ell)$$

then

$$We = K_3(1 + \rho_v/\rho_\ell), \qquad 2\pi < K_3 < 3\pi. \tag{5.9}$$

If we can assume that $\rho_v << \rho_\ell$ (for example, with water at 100°C, $\rho_v/\rho_\ell = 6.24 \times 10^{-4}$), then

$$We = K_3, \qquad 2\pi < K_3 < 3\pi. \tag{5.10}$$

Thus, according to this analysis, growing instabilities and entrainment will begin when $We > 2\pi$ rather than $We = 1$ as has been suggested in the past. However, if Cotter's[9] Weber number is interpreted as in Equation 2.16, then there is agreement that growing instabilities and entrainment occurs when $We > 2\pi$.

5.1.2 Wave Speed Relationship

The initiation of wave instabilities may be further described by determining the wave speed and wave length at the onset of ripple waves. The wave speed, C, may be most easily determined by a coordinate system with the x-axis at the averaged liquid-vapor interface. Again, a sinusoidal wave is assumed to exist at the liquid-vapor interface as shown in Figure 10.

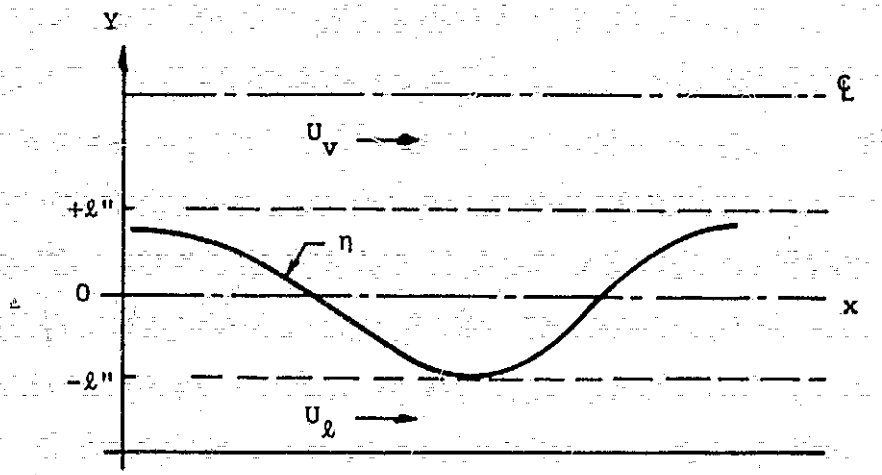

Fig. 10. Wave speed analysis coordinate system.

The analysis, given in Appendix A, describes the wave speed by the following relationships.

$$C = \frac{(\rho_\ell U_\ell + \rho_v U_v)}{\rho_\ell + \rho_v} \pm \left[C_o^2 - \frac{\rho_v \rho_\ell (U_v + U_\ell)^2}{(\rho_\ell + \rho_v)^2} \right]^{1/2} \tag{5.11}$$

where

$$C_o^2 = \frac{\lambda}{2\pi} \frac{(\rho_\ell - \rho_v)}{(\rho_\ell + \rho_v)} + \frac{2\pi}{\lambda} \frac{\sigma}{(\rho_\ell + \rho_v)} \tag{5.12}$$

C_o is the wave speed of a traveling ripple wave in a quiet fluid where $U_v = U_\ell = 0$, that is, like that observed by a pebble thrown in a still pond.

From Equation 5.11, we can see that the wave will be unstable if

$$\rho_\ell \rho_v \left[\frac{U_{v\ell}}{\rho_\ell + \rho_v} \right]^2 > C_o^2 \tag{5.13}$$

The value of λ for which C_o is a minimum may be designated by λ_{rip} and corresponds to the point of onset of ripple waves. This value of λ_{rip} can be determined by differentiating Equation 5.11 with respect to λ and setting it equal to zero. We then find that the value of λ_{rip} is

$$\lambda_{rip} = 2\pi\sqrt{\frac{\sigma}{(\rho_\ell - \rho_v)}} \tag{5.14}$$

and the corresponding minimum value of C_o is

$$C_{c_{rip}} = \left[\frac{2\sigma\ (\rho_\ell - \rho_v)}{(\rho_\ell + \rho_v)^2}\right]^{1/2} . \tag{5.15}$$

For a flowing vapor or gas to cause waves on a liquid surface, its speed must be greater than or equal to the minimum ripple wave speed, that is, $U_{v\ell} > C_{o_{rip}}$. As the vapor velocity is increased, the wave speed and amplitude will increase correspondingly, decreasing in wavelength until $\lambda_o = \lambda_m$ (where $K_3 = 3\pi$) is reached, where we assumed in the analysis that the entrainment is well developed.

5.1.3 Unstable Wavelength

From Equation 5.13, the liquid film will be unstable if

$$\rho_\ell\rho_v\left(\frac{U_{v\ell}^2}{\rho_\ell + \rho_v}\right)^2 > C_o^2 . \tag{5.13}$$

and we know there is a dominant wavelength given by Equation 5.6

$$\lambda_o = \frac{K_3\sigma}{\rho_v\ U_{v\ell}^2}\left(1 + \frac{\rho_v}{\rho_\ell}\right) \qquad 2\pi < K_3 < 3\pi \tag{5.6}$$

after rearranging and dividing through both sides by $(\rho_\ell + \rho_v)$ and dropping the λ_o subscript, we get

$$\rho_\ell\rho_v\left(\frac{U_{v\ell}}{\rho_\ell + \rho_v}\right)^2 = \frac{\sigma K_3}{\lambda(\rho_\ell + \rho_v)} . \tag{5.16}$$

The righthand side of Equation 4.16 gives the value of $\rho_\ell\rho_v\left(\frac{U_{v\ell}}{\rho_\ell + \rho_v}\right)^2$ in term of the wave length λ.

Thus, the incipient entrainment wavelength can be found by using Equations 5.12 and 5.16 satisfying the relationship 5.13. This can be done by plotting C_o^2 vs. λ and

$$\frac{\sigma K_3}{\lambda(\rho_\ell + \rho_v)} \quad \text{vs.} \quad \lambda$$

the intersection point between two curves gives the value of incipient entrainment wavelength, λ_{en}, as shown in figures 11 and 12 for ammonia at 203 K and 320 K respectively.

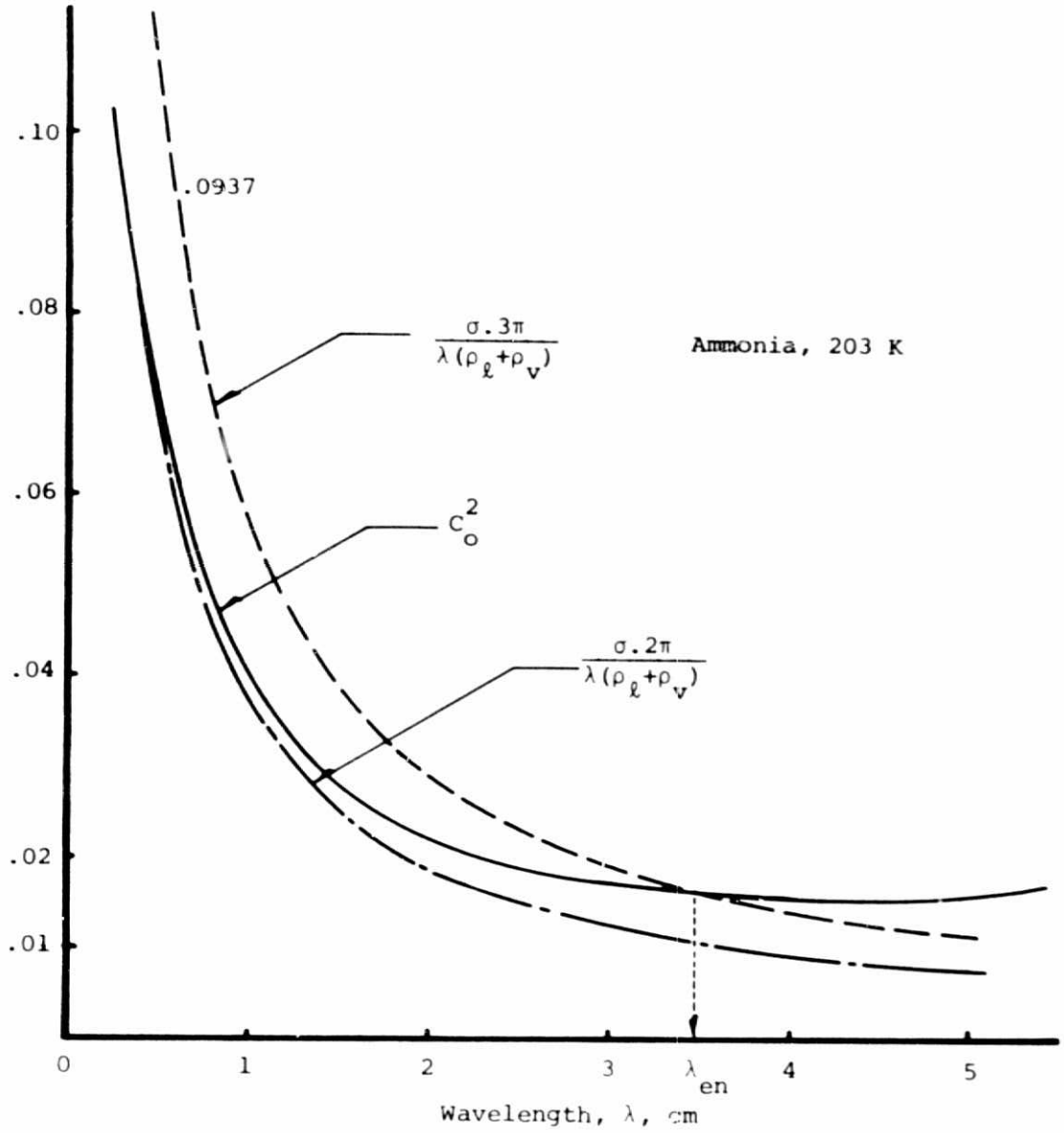

Fig. 11. Entrainment wavelength for ammonia, T = 203 K

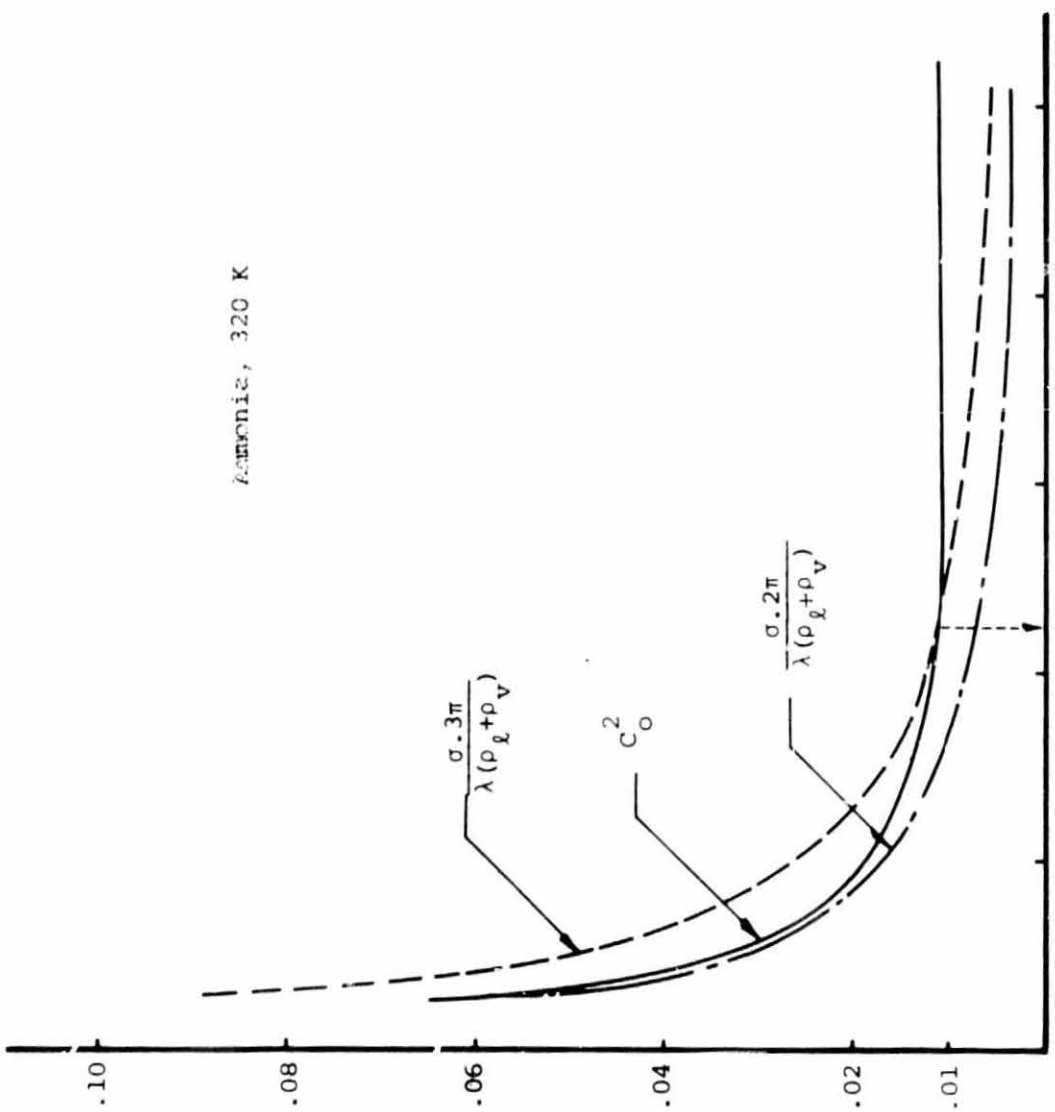

Fig. 12. Entrainment wavelength for ammonia, T = 320 K

6.0 ENTRAINMENT HEAT FLUX

The entrainment is assumed to be developed as the result of the liquid surface dynamic instability at wavelength

$$\lambda_{en} = \frac{3\pi\sigma}{\rho_v U_{v\ell}^2} \left(1 + \frac{\rho_v}{\rho_\ell}\right) \tag{6.1}$$

thus,

$$U_{v\ell} = \left[\frac{3\pi\sigma}{\rho_v \lambda_{en}} \left(1 + \frac{\rho_v}{\rho_\ell}\right)\right]^{1/2} \tag{6.2}$$

For relatively low liquid velocities the following approximation holds,

$$U_{v\ell} \simeq U_v \tag{6.3}$$

and because

$$\frac{\dot{Q}}{A_v} = \rho_v U_v h_{fg}$$

$$\text{so} \quad \left(\frac{\dot{Q}}{A_v}\right)_{en} \simeq \rho_v U_{v\ell} h_{fg} \tag{6.4}$$

By combining Equations 6.2 and 6.4, the incipient entrainment heat flux can then be determined by,

$$\left(\frac{\dot{Q}}{A_v}\right)_{en} \simeq \left[\frac{3\pi\sigma}{\lambda_{en}} \left(1 + \frac{\rho_v}{\rho_\ell}\right)^{1/2}\right] h_{fg} \tag{6.5}$$

Equation 6.5 has been plotted along with the sonic heat flux limit and the wicking limit heat flux including counterflow shear effects for water, freon-11, ammonia, and methane in Figures 13 through 16, respectively. The equation used for the sonic heat flux limit is that given by Levy[18]

$$\left(\frac{\dot{Q}}{A_v}\right)_s = \frac{\rho_v C_s h_{fg}}{2\sqrt{k+1}} \tag{6.6}$$

where ρ_v and C_s are the vapor density and speed of sound evaluated at the evaporator entrance temperature and $k = c_p/c_v$ is the ratio of specific heats. Equations 2.4 through 2.13 given by Schlitt, et al.[7] were combined

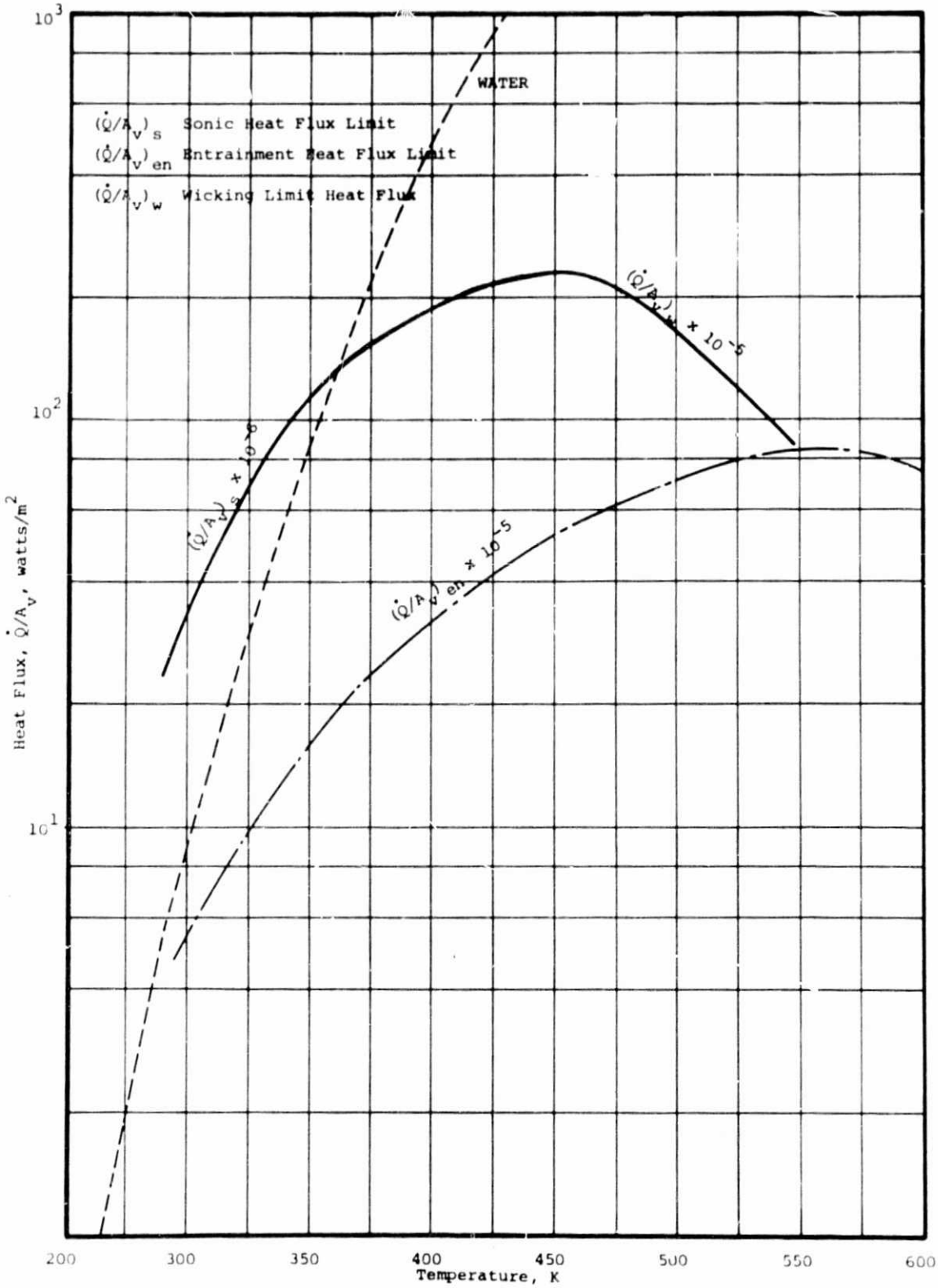

Fig. 13. Performance heat flux limits for water in an axial groove heat pipe.

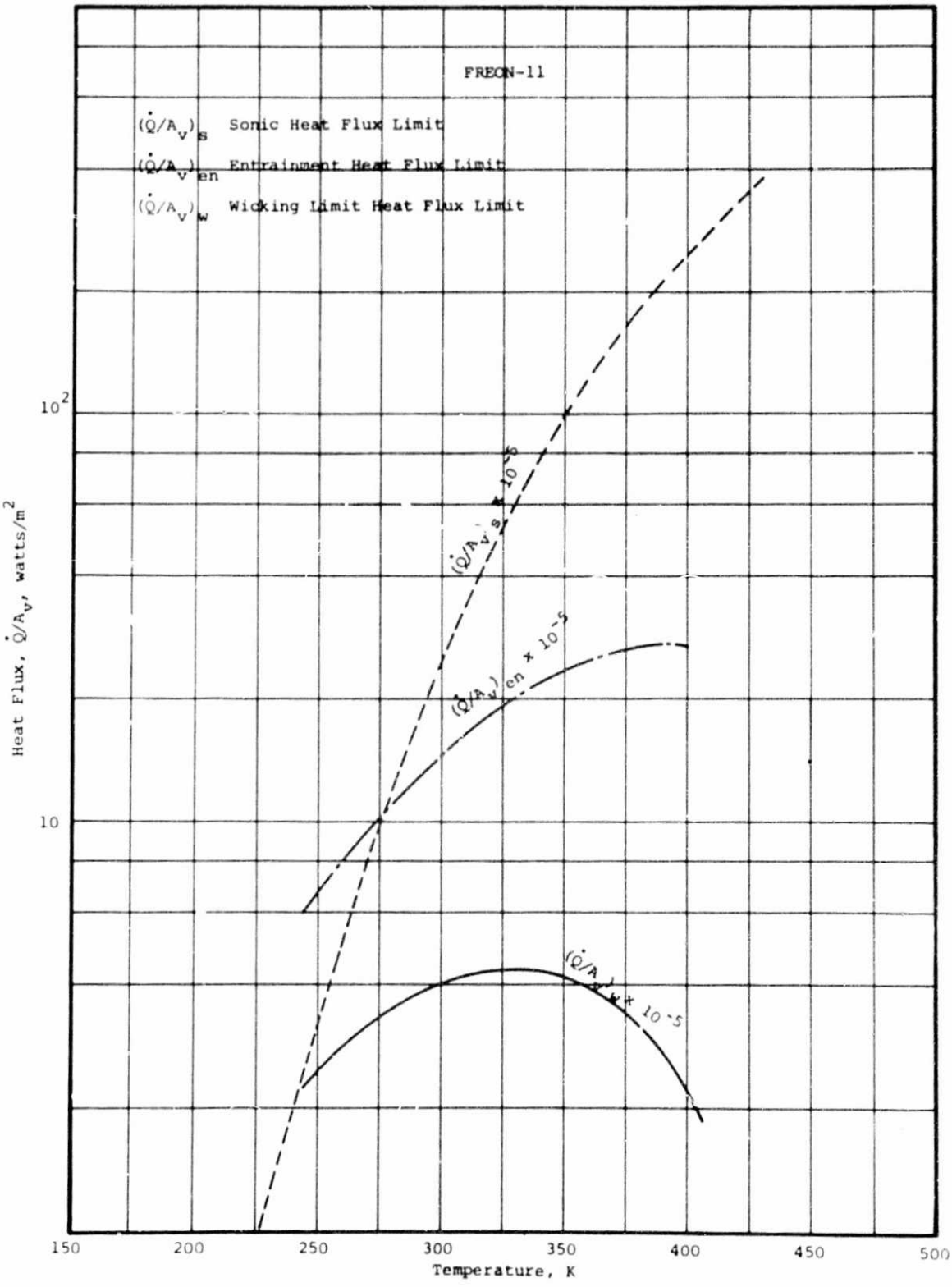

Fig. 14. Performance heat flux limits for freon-11 in an axial groove heat pipe

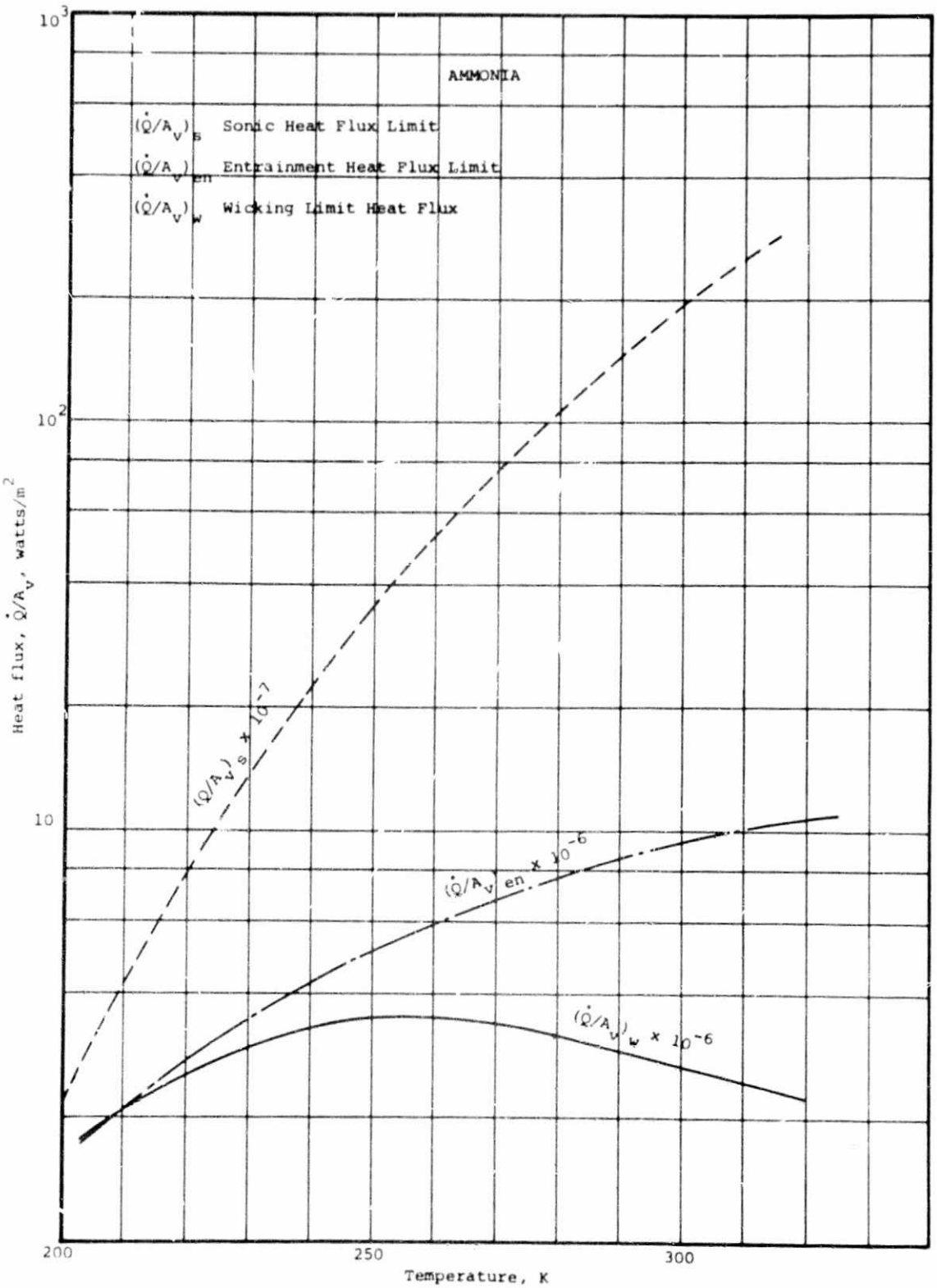

Fig. 15. Performance heat flux limits for ammonia in an axial groove heat pipe

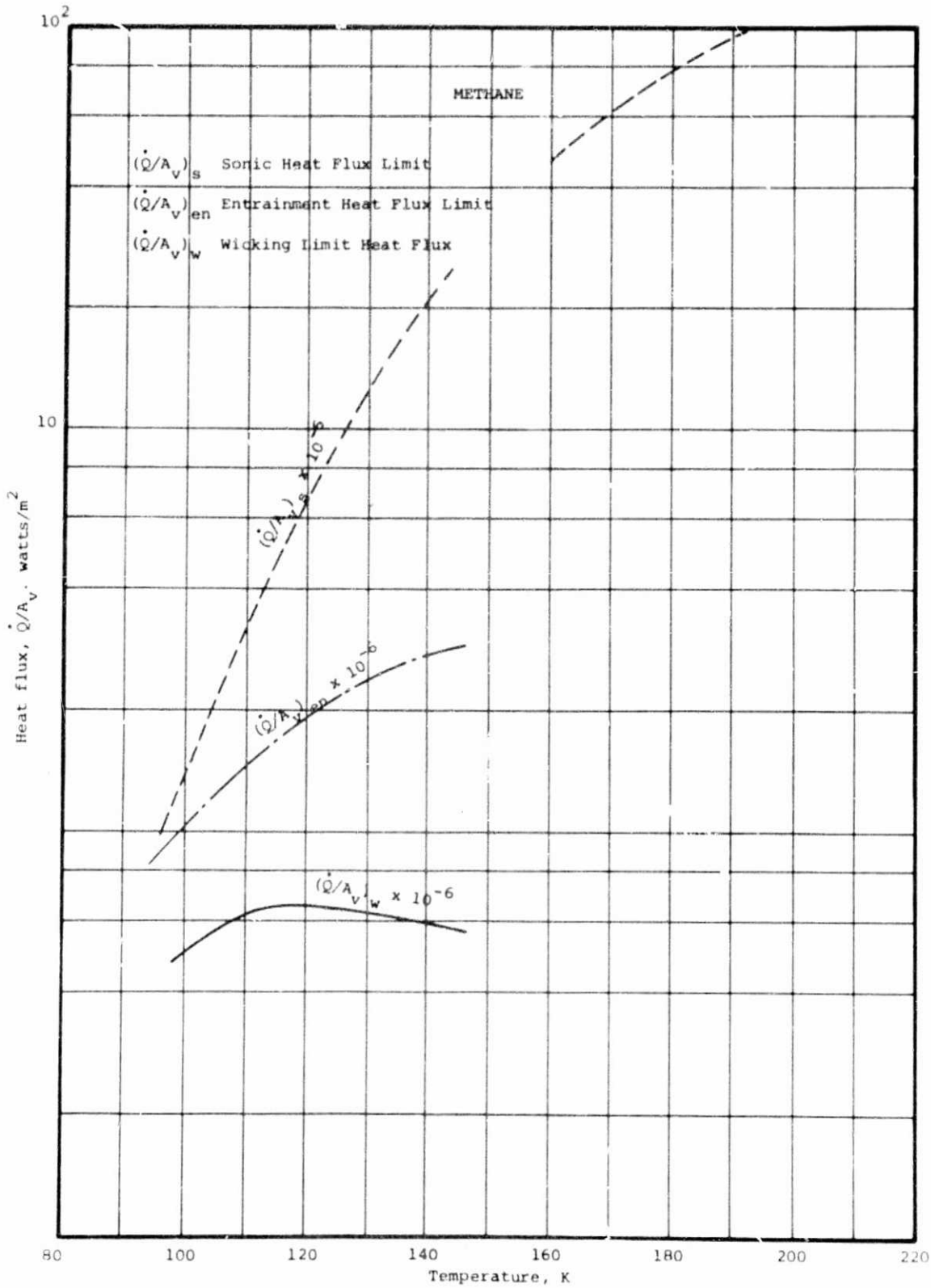

Fig. 16. Performance heat flux limits for methane in an axial groove heat pipe

to give,

$$\dot{Q}_w = \frac{N_\ell K A_\ell}{r_p L_{eff}} \left[\frac{8}{3} \frac{\nu_v}{\nu_\ell} \frac{(w/D_v)^2}{(1+s/w)} + 1 + \frac{8}{3} \frac{\nu_v}{\nu_\ell} \frac{K A_\ell}{D_v^2 A_v} \right]^{-1} \qquad (6.7)$$

which gives the wicking limit heat transfer rate including vapor-liquid counter flow shear effects. The axial groove heat pipe dimensions given in Figure 1 were used in these calculations.

In the Figures 13 through 16 it is apparent that the sonic limit heat flux is considerably higher than the other limits for all the fluids. However, since the wicking limit is more sensitive to the liquid properties than the other limits considered here, the wicking limit exceeds the entrainment limit for water as shown in Figure 13. For freon-11, ammonia, and methane, which are less effective working fluids (N_ℓ is lower), the wicking limit is the lowest limit. In all cases, the limits are lowest at low temperature where vapor densities are low and vapor velocities are high. This low temperature condition occurs during startup and causes relatively large pressure losses and low heat transfer rates.

7.0 CONCLUSIONS AND RECOMMENDATIONS

According to the analysis presented in this report, using the linearized instability theory, wave instabilities grow and entrainment begins when $2\pi < We < 3\pi$ rather than at $We \geq 1$ as suggested in the past. Here the Weber number is defined as $We \equiv (\rho_v U_{v\ell}^2 \lambda_o)/\sigma$ and λ_o, which is the wavelength of the growing instable wave defined by Equation 5.6, is used as the characteristic dimension in place of d. It should be noted that this result is identical to that suggested by Cotter[9] in Equation 2.15 if both sides of his equation are multiplied by 2π to give Equation 2.16. Cotter further stated that $\lambda/2\pi = d$, is a characteristic dimension which is a geometric property of the wick surface. Additional experimental data is needed in order to determine any relationship between d and the wick surface geometry, particularly for axial groove heat pipes.

The effect of the counter flow shear force between the vapor and liquid is to create an additional pressure drop, given by $\Delta p_{\ell,v}$ in Equation 2.7, which reduces the overall heat transfer rate of the heat pipe, given by Equation 6.7. If wicking forces are sufficiently high, as they are for water, the wicking limit can exceed the entrainment limit which was shown in figure 13. Thus, according to the calculations plotted in figure 13 for the axial groove heat pipe shown in figure 1, it is possible to observe entrainment of water since the entrainment limit occurs before the wicking limit. However, for this axial groove heat pipe operating with ammonia, freon-11, or methane, as shown in figures 14, 15, and 16, the wicking limit would be reached before the entrainment limit and entrainment would never be attained.

The entrainment limit heat flux is given by Equation 6.5, the entrainment velocity by Equation 6.2, and the entrainment wavelength by Equation 6.1. The onset of ripple waves occurs at a wave speed and wavelength given by Equations 5.15 and 5.14, respectively.

Further experimental measurements of the counterflow shear effects and the entrainment limits need to be made and compared to the values predicted by the equations given in this report.

8.0 References

1. K. T. Feldman, Jr., Editor, Heat Pipe Technology Bibliography, The University of New Mexico, Albuquerque, 1974.

2. A. Bähr, E. Burck, and W. Hufschmidt, "Liquid-Vapor Interaction and Evaporation in Heat Pipes," Paper D-6, 2nd International Conference on Thermionic Electric Power Generation, May 27-31, 1968.

3. W. Hufschmidt, E. Burck, G. DiCola, and H. Hoffman, "Der Einfluss der Scherwirkung des Dampfstromes auf den laminaren Flüssigkeitsstrom in Kapillaren von Wärmerohren," Wärme-und Stoffübertragung, Bd. 2 (1969) S. 222-239.

4. G. DiCola, "Soluzione Analitica, a mezzo della transformata di Fourier di un problema flusso in a canale rettangolare," EURATOM, C.C.R., Ispra, Italy, C.E.T.I.S., 1968.

5. L. W. Florschuetz, "Estimates of the Significance of Vapor-Liquid Shear Interaction on the Performance of Heat Pipes with Open Rectangular Groove Capillary Structures," Los Alamos Scientific Laboratory, N-5 Technical Memorandum No. 172, Los Alamos, New Mexico, August 10, 1970.

6. P. Zimmermann, "Einfluss der Dampfströmung auf das instationäre Betriebsverhalten von Wärmerohren," Dissertation, Universität Stuttgard, (1972)

7. K. R. Schlitt, J. P. Kirkpatrick, and P. J. Brennan, "Parametric Performance of Extruded Axial Grooved Heat Pipes from 100° to 300°K," AIAA Paper No. 74-724, Thermophysics and Heat Transfer Conference, Boston, Massachusetts, July 15-17, 1974.

8. G. B. Wallis, One-Dimensional Two-Phase Flow, McGraw-Hill Book Company, 1969.

9. T. P. Cotter, "Heat Pipe Startup Dynamics," 1967 IEEE Thermionic Conversion Specialist Conference, Palo Also, California, October 30 - November 1, 1967, pp. 344-348.

10. J. E. Kemme, "High Performance Heat Pipes," 1967 IEEE Thermionic Conversion Specialist Conference, Palo Alto, California, October 30 - November 1, 1967, pp. 355-358.

11. T. J. Hanratty and J. M. Engen, "Interaction Between a Turbulent Air Stream and a Moving Water Surface," AIChE Journal, Vol. 3, September 1957.

12. T. J. Hanratty and A. Hershamn, "Initiation of Roll Waves," AIChE Journal, Vol. 7, September 1961.

13. Vaughn Cornish, Waves of the Sea and Other Water Waves, T. Fisher Unwin, London, England, 1910.

14. H. Jeffreys, Proceedings of the Royal Society, A107, 189, 1925.

15. G. B. Wallis, J. M. Turner, I. Bemberis, and D. Kaufman, AEC Report NYO-3114-4, 1964.

16. G. F. Hewitt, N. S. Hall-Taylor, Annular Two-Phase Flow, Pergamon Press, 1970.

17. F. E. Tippets, "Analysis of the Critical Heat-Flux Condition in High-Pressure Boiling Water Flows," Journal of Heat Transfer, Trans. ASME, February 1964, pp. 23-38.

18. E. K. Levy, "Theoretical Investigation of Heat Pipes Operating at Low Vapor Pressures," ASME Transactions - Journal of Engineering for Industry, November 1968, pp. 547-552.

19. N. E. Kochin, I. A. Kible, N. V. Roze, Theoretical Hydrodynamics, John Wiley, 1964.

9.0 APPENDIX A

APPENDIX A

Detailed Analysis of Wave Instability

Here an original analysis of the counterflow shear wave instability is presented. For this analysis a fixed coordinate system is assumed where a liquid film is moving at speed u_ℓ and a vapor moving over it at speed u_v as shown in Figure A1.

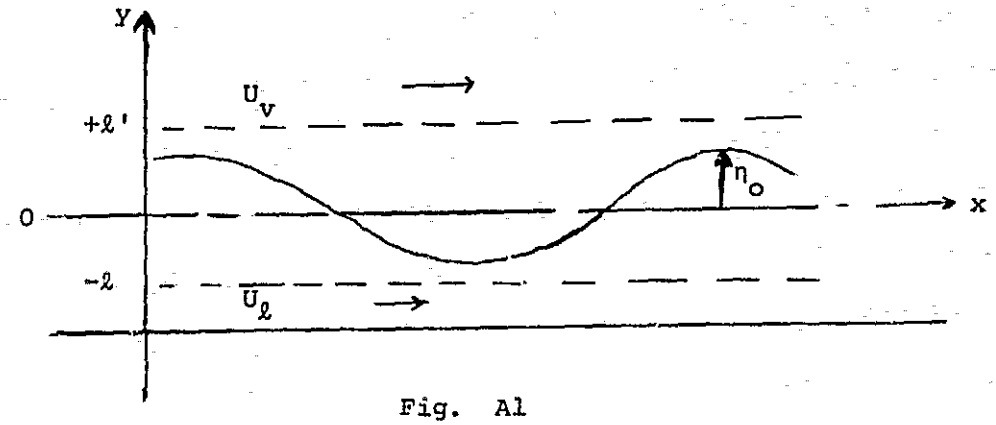

Fig. A1

The liquid and vapor flows may be represented by a velocity potential, $\phi = ux$, plus a perturbation term, ϕ', to account for the waves,

$$\phi_v = u_v x + \phi' \tag{A.1a}$$

$$\phi_\ell = u_\ell x + \phi'_\ell \tag{A.1b}$$

The corresponding boundary conditions are

$$\phi'_v = 0 \text{ at } y = + \ell'' \tag{A.2a}$$

and

$$\phi'_\ell = 0 \text{ at } y = - \ell'' \tag{A.2b}$$

The use of velocity potentials requires that the flow is irrotational; that is, the perturbation terms, ϕ', must satisfy the Laplace's equation,

$$\frac{\partial^2 \phi'}{\partial x^2} + \frac{\partial^2 \phi'}{\partial y^2} = 0 \qquad (A.3)$$

The perturbation terms may then be described by a sinusoidal term,

$$\phi'(x,y,t) = Y(y) \sin \frac{2\pi}{\lambda} (x - Ct) \qquad (A.4)$$

Introducing A.4 into A.3 we get

$$\frac{d^2 Y}{dy^2} - \left(\frac{2\pi}{\lambda}\right)^2 Y = 0$$

where the solution is

$$Y = Ae^{\frac{2\pi}{\lambda} y} + Be^{-\frac{2\pi}{\lambda} y}$$

thus Equation A.4 becomes

$$\phi'(x,y,t) = (Ae^{\frac{2\pi}{\lambda} y} + Be^{-\frac{2\pi}{\lambda} y}) \sin \frac{2\pi}{\lambda} (x-Ct) \qquad (A.5)$$

Applying the boundary condition A.2a to ϕ' we get

$$\phi'_v(x,y,t) = D \sin \frac{2\pi}{\lambda} (y-\ell'') \sin \frac{2\pi}{\lambda} (x-Ct) \qquad (A.6a)$$

and the boundary condition A.2b gives

$$\phi'_\ell (x,y,t) = E \sinh \frac{2\pi}{\lambda} (y+\ell'') \sin \frac{2\pi}{\lambda} (x-Ct) \qquad (A.6b)$$

where D and E are constants.

The forms of Equations A.6 indicate that the displacement η has a sinusoidal form as,

$$\eta = \eta_o \cos \frac{2\pi}{\lambda} (x-Ct) \qquad (A.7)$$

The linearized kinematic conditions across the liquid-vapor interface are

$$\frac{\partial \eta}{\partial t} + u_v \frac{\partial \eta}{\partial x} = \frac{\partial \phi'_v}{\partial y} \tag{A.8a}$$

$$\frac{\partial \eta}{\partial t} + u_\ell \frac{\partial \eta}{\partial x} = \frac{\partial \phi'_\ell}{\partial y} \tag{A.8b}$$

Substituting Equations A.6a, A.6b, and A.7 into A.8a and A.8b respectively, we get

$$D = \frac{\eta_o (C-u_v)}{\cosh \frac{2\pi}{\lambda} (y-\ell")} \tag{A.9a}$$

and

$$E = \frac{\eta_o (C-u_\ell)}{\cosh \frac{2\pi}{\lambda} (y+\ell")} \tag{A.9b}$$

The dynamic pressure gradient condition across the interface in linearized form is

$$p'_\ell - p'_v = - \sigma \frac{\partial^2 \eta}{\partial x^2} \tag{A.10}$$

where p' is the pressure perturbation and σ is the surface tension.

The pressure, p', may be calculated from the linearized Bernoulli equation

$$\frac{p'}{\rho} = \frac{\partial \phi'}{\partial t} + u \frac{\partial \phi'}{\partial x} - g\eta \tag{A.11}$$

Substituting Equation A.11 into A.10, we get

$$-\rho_v \left(\frac{\partial \phi'_v}{\partial t} + u_v \frac{\partial \phi'}{\partial \chi} - g\eta\right) + \rho_\ell \left(\frac{\partial \phi'_\ell}{\partial t} + u_\ell \frac{\partial \phi'_\ell}{\partial x} - g\eta\right)$$

$$= - \sigma \frac{\partial^2 \eta}{\partial x^2} \tag{A.12}$$

Now we substitute Equations A.6a, A.6b and A.7 into A.12 and eliminate D using A.9a, E using A.9b, and η_o, we get

$$\rho_v \quad (-C+u_v)(C-u_v)\tanh\frac{2\pi}{\lambda}(y-\ell'')$$

$$\rho_\ell \quad (-C+u_\ell)(C-u_\ell)\tanh\frac{2\pi}{\lambda}(y+\ell'') \quad -\frac{g\lambda}{2\pi}(\rho_\ell-\rho_v) = \sigma\frac{2\pi}{\lambda}$$

The above equation may be simplified with very little error, as did Tippits [17] by recognizing that $\ell'' \cong .4\ \lambda_o$ and y is very small so that the tanh terms are nearly equal to 1, as

$$\rho_v\ (C-u_v)^2 + \rho_\ell\ (C-u_\ell)^2 - \frac{g\lambda}{2\pi}(\rho_\ell - \rho_v) - \frac{2\pi\sigma}{\lambda} = 0 \qquad \text{(A.13)}$$

Rearranging Equation A.13 and solving for C, we get

$$C = \frac{(\rho_\ell u_\ell+\rho_v u_v)}{(\rho_\ell+\rho_v)} \pm \left[C_o^2 - \frac{\rho_v\rho_\ell(u_{v\ell})^2}{(\rho_\ell+\rho_v)^2}\right]^{1/2} \qquad \text{(A.14)}$$

where

$$C_o^2 = \frac{g\lambda}{2\pi}\frac{(\rho_\ell-\rho_v)}{(\rho_\ell+\rho_v)} + \frac{2\pi\sigma}{\lambda(\rho_\ell+\rho_v)} \qquad \text{(A.15)}$$

Note that C_o is the wave speed of a traveling ripple wave in a quiet fluid where $u_v = u_\ell = 0$.

From Equation A.14 we can see that the flow will be unstable and waves will be formed if

$$\rho_\ell\rho_v\frac{(u_v+u_\ell)^2}{(\rho_\ell+\rho_v)} > C_o^2$$

or rearranging

$$\rho_\ell\rho_v\left(\frac{u_{v\ell}}{\rho_\ell+\rho_v}\right)^2 > C_o^2 \qquad \text{(A.16)}$$

The magnitude of C given by Equation A.14 varies with λ as is shown in Figure 5.3. The value of λ for which C is a minimum may be designated λ_{rip} and corresponds to the point of onset for ripple waves. This value of λ_{rip} can be determined by differentiating equation A.15 with respect

to λ and setting it equal to zero.

Solving for λ_{rip} we get

$$\lambda_{rip} = 2\pi \sqrt{\frac{\sigma}{(\rho_\ell - \rho_v) g_c}} \tag{A.17}$$

The corresponding minimum value of C_o is

$$C_{o\ rip} = \left[\frac{2\sigma g_c (\rho_\ell - \rho_v)}{(\rho_\ell + \rho_v)^2} \right]^{1/2} \tag{A.18}$$

For a flowing vapor to cause waves on a liquid surface its speed must be greater than or equal to the minimum ripple wave speed, that is, $u_v \geq C_{o\ rip}$.

We are interested in waves which are more unstable than the weak ripple waves, we are therefore interested in waves which have a smaller wave length than ripple waves, that is, we are interested in waves with $\lambda \leq \lambda_{rip}$. For small values of λ the gravity term in equation A.15 for C_o may be neglected, and then solving for λ from Equation A.16 we get

$$\lambda > \frac{2\pi\sigma}{\rho_v u_{v\ell}^2} \left(1 + \frac{\rho_v}{\rho_\ell}\right) \tag{A.19}$$

which is identical to Equation 4.3 given by Tippets [17]!